



## Characterization of metal-bearing diesel nanoparticles using single-particle mass spectrometry

D. Lee<sup>a</sup>, A. Miller<sup>b</sup>, D. Kittelson<sup>c</sup>, M.R. Zachariah<sup>d,\*</sup>

<sup>a</sup>*School of Mechanical Engineering, Pusan National University, Pusan 609 735, Korea*

<sup>b</sup>*NIOSH/Spokane Research Lab, 315 E Montgomery, Spokane, Washington 99208*

<sup>c</sup>*Department of Mechanical Engineering, University of Minnesota, 111 Church Street S.E., Minneapolis, Minnesota 55455*

<sup>d</sup>*Department of Chemistry, University of Minnesota, 111 Church Street S.E., Minneapolis, Minnesota 55455*

Received 25 April 2004; received in revised form 6 April 2005; accepted 7 April 2005

### Abstract

Acute and chronic health effects have been associated with diesel particulate matter (DPM). Since both ultrafine particles and metals have been implicated in this correlation, we are conducting investigations to characterize the metal content of diesel nanoparticles. For this study, DPM was generated by a 1.5 l engine and ferrocene was added to the fuel to raise the level of metal in the system. The exhaust particles were analyzed in real time using a recently developed single-particle mass spectrometer (SPMS) that has the capability of ablating each particle down to its elemental constituents, thereby yielding the relative mass of elements in each particle. Particle-size calibration of the instrument was achieved by correlating the SPMS signal intensity with measured DPM size. Using this approach, we present size- and composition-resolved elemental species distributions for both the nuclei mode and ultrafine portion of the accumulation mode of DPM. Results show that when the fuel is doped with ferrocene, iron-rich nanoparticles are formed and their number and size increase with level of doping. Larger iron-bearing particles are also formed, but it is observed that the metal to carbon ratios increase for smaller particle sizes. Hydrogen to carbon ratios were measured as a function of particle size, which allowed us to determine the relative amounts of organic carbon and elemental carbon in the particles and showed that the hydrogen to carbon ratios increase for

\* Corresponding author. Present address: University of Maryland, College Park, USA. Tel.: +1 301 405 4311; fax: +1 301 314 9477.

*E-mail address:* [mrz@umd.edu](mailto:mrz@umd.edu) (M.R. Zachariah).

smaller sized particles. The combined results are used to discuss the effects of metal doping level and engine load on particle nucleation and mechanisms of DPM formation.

© 2005 Elsevier Ltd. All rights reserved.

*Keywords:* Single-particle mass spectrometry; Diesel particulate matter (DPM); Nanoparticles; Iron nanoparticles; Homogeneous nucleation; Metal; Mechanism of DPM formation

---

## 1. Introduction

### 1.1. Background

It is known that diesel engines produce a tri-modal size distribution of diesel particulate matter (DPM) (Kittelson, 1998). The newer “cleaner” engines, although they produce less mass of particles, can sometimes produce a greater number of nano-size particles (Bagley, Baumgard, Gratz, Johnson, & Leddy, 1996; Kittelson, Johnson, & Watts, 2002; Kittelson et al., 2000), although many new engines reduce number and mass simultaneously. This “nuclei mode” of particles is quite variable and can be attributed in many cases to the self-nucleation of volatile species during the dilution and simultaneous cooling of the exhaust aerosol as it exits the tailpipe. It has also been shown that some nanoparticles may form prior to dilution and that this phenomenon can be enhanced by introducing trace amounts of metals into the fuel (Du, Kracklauer, & Kittelson, 1998; Higgins, Jung, Kittelson, Roberts, & Zachariah, 2002). The increase in nuclei-mode particles is thought not to be a direct function of how “clean” the engine is, but rather to depend on the ratio between carbon (soot) and the nucleating species.

The dynamics of particle formation during and after combustion is a topic of much interest and investigation. A recent summary of the diesel combustion process (Flynn et al., 1999) describes how the fuel jet quickly disintegrates as it exits the nozzle and vaporizes as it entrains hot air, subsequently forming a plume of fuel-vapor and air mixture with a diffusion flame at its periphery. It has been shown that soot precursors originate from partial oxidation of fuel in the fuel-rich region of this plume. It is postulated that within the plume, the precursors form soot primary particles that are spherical. Such particles begin to agglomerate and subsequently encounter the diffusion flame and are mostly oxidized at temperatures around 2500 K, but it is thought that some survive due to localized quenching and remain in the combustion chamber. As the piston moves downward, the system cools rapidly. At this stage, if there are other non-volatile gaseous species (such as metals) with very high concentrations, they will deposit on the carbon particles or may alternatively self-nucleate if the rapid cooling drives their saturation ratios high enough. As the resulting aerosol travels through the exhaust system, further cooling causes semi-volatile species such as polycyclic aromatic hydrocarbons (PAH's) to condense onto the particles. When the aerosol exits the tailpipe, it again cools rapidly and other more volatile species condense suddenly and/or self-nucleate into nanoparticles. The resulting complex mixture of particles is what we call DPM.

Both chronic and acute health effects have been shown to be associated with DPM and one theory suggests that the ultrafine and nano-sized particles, i.e. particles less than about 100 nm in diameter, may play a key role in this (Donaldson & Stone, 2003; Utell & Frampton, 2000). Although techniques have been developed to characterize the size of such small particles (Abdul-Khalek, Kittelson, & Brear, 1999; Abdul-Khalek, Kittelson, Graskow, Wei, & Brear, 1998; Kittelson, 1998), more important factors resulting in adverse health effects may be related to their chemical composition (Costa & Dreher, 1997).

Traditionally, the chemical analysis of aerosols requires sample collection followed by off-line analysis. Such analysis can suffer from artifacts arising from reactions within the collected sample itself or between the sample and the substrate (Appel & Tokiwa, 1981) and can often only give results corresponding to bulk properties. Several newer methods utilizing mass spectrometry for chemical analysis of single particles provide simultaneous size information (Suess & Prather, 1999), but most such mass spectrometers employ light scattering for sizing the DPM. Since the intensity of scattered light reduces sharply for particles below 200 nm, the lower limit of measurable particle size is typically around 200 nm. Tobias, Kooiman, Docherty, and Ziemann (2000) reported that a thermal desorption mass spectrometer could simultaneously measure the size and chemical composition of ultrafine particles, but their evaporation method (electrical heater in quadrupole cell) allows only the measurement of the volatile species coating the DPM, or the self-nucleated particles of sulfate or organic carbon (OC). The issue of chemical composition and its links to particle formation scenarios is, therefore, complex and remains elusive. We are now proposing that our recently developed single-particle mass spectrometer (SPMS), employing a much stronger laser, may overcome the above current limitations.

Metals in diesel exhaust may originate from sources such as trace metals in the fuel, the use of metallic fuel additives for enhancing regeneration of diesel particulate filters (Stratakis & Stamatelos, 2003), or from lube oil additives that enter the combustion chamber via reverse blow-by of the piston rings. The role of such metals in the chemistry of DPM formation remains a challenging topic of investigation. The research reported here aims at providing insight into the formation of metal-rich nanoparticles via self-nucleation as well as the overall distribution of metals across a wider range of particle sizes due to adsorption, condensation and coagulation.

## 1.2. Research approach

The main goals of this work are to quantify the amount of metal in various sizes of DPM and to investigate how metal levels during combustion may affect the chemistry of particle formation. The research approach taken was to use a diesel engine to generate exhaust particles and to dope the fuel supply with ferrocene to introduce metal (iron) into the combustion process. The resulting iron-bearing diesel exhaust particles were analyzed using a recently developed SPMS that is capable of determining the elemental composition of both fine and ultrafine particles (Mahadevan, Lee, Sakurai, & Zachariah, 2002), and as we show in this paper, the particle size may also be derived from the same measurement.

Lab testing entailed running the diesel engine and routing a sample of the diluted exhaust aerosol to a scanning mobility particle sizer (SMPS) and to the SPMS for analysis. (Note the similarity in acronyms.) The latter generated mass spectra for large numbers of individual particles. Subsequent analysis of the spectral data provided insight into not only the elemental composition of particles that make up the DPM aerosol but also the size preference of the elements. Additional offline particle analysis was conducted using transmission electron microscopy (TEM) and energy dispersive spectroscopy (EDS). The offline results are covered only briefly, as the bulk of that work will be submitted as a sequel to this paper.

The following section describes the experimental setup including details about the SMPS, SPMS and its aerodynamic lens inlet, the data processing software and the engine and sampling arrangement. The subsequent section includes various presentations of the SPMS data that show elemental composition of particles, as well as discussion of those results. In that section, three distinct classes of particles are identified and data presented which support that observation. The final section summarizes the highlights of the data analysis.

## 2. Experimental setup and procedures

### 2.1. Diesel particle generation

The source of diesel particulate for this work was an Onan-Cummins “QuietDiesel” genset powered by a three cylinder, 1.5 l Isuzu engine. This unit is capable of providing 10 kW of continuous AC power at a fuel flow rate of about 4 kg/h. In order to maintain a steady 60 Hz of AC current from the generator, the fuel flow to the engine is controlled by an electronic governor actuator that maintains a constant engine speed of 1800 rpm. The load on the engine is provided by loading the generator outlet with a resistive load bank made by the Simplex Company. For most of our experiments, the engine was run at two conditions, i.e. no-load and 6 kW load. The corresponding fuel flow rates were 1.0 and 2.25 kg/h. It should be noted that the size distribution of particles generated by this relatively small engine varies somewhat from that of typical heavy duty engines. Under normal operating conditions, it produces no discernable nuclei mode and the accumulation mode decreases with engine load rather than increases as it does for most larger engines.

The particulate matter for SPMS analysis is drawn approximately isokinetically from the tailpipe as shown in Fig. 1. The 3.8 cm diameter exhaust line is connected to a fume hood system via a 10 cm diameter pipe, and a 20 cm long, 3 mm-ID stainless-steel probe draws a sample about 15 cm from the muffler exit at a flow rate of about 5 lpm. The probe is inserted through the tailpipe wall and directed into the exhaust stream. The opposite end of the probe is attached to the inlet of an AirVac-TD260H vacuum pump that acts as an ejector dilutor as described in previous work (Abdul-Khalek et al., 1999). The dilutor is fed a supply of 30 psi (200 kPa) dry air at room temperature. Cold-flow calibration, using a bubble flow meter at the dilutor inlet and a rotameter at the outlet, yielded a dilution ratio of approximately 10:1 for this setup. For measurements of particle size distribution with the SMPS, the flow was further diluted as shown in Fig. 1, using a second ejector dilutor. Note that all SMPS data in this report have been dilution corrected to represent tailpipe conditions. Note that the use of ejector dilutors has been well

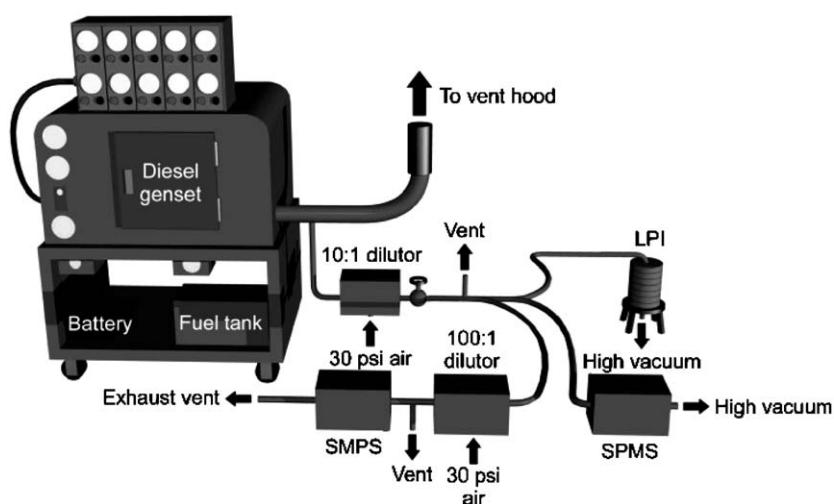


Fig. 1. Sampling and dilution of DPM using exhaust probe and ejector dilutor.

documented (Abdul-Khalek et al., 1999), and is an effective way to mimic the dilution and quenching that occurs downstream of the tailpipe under real operating conditions. To rule out the possibility of further nucleation or condensation and to verify the stability of particle size distributions for our setup, a series of measurements were made using a variable residence time dilution tunnel. Results revealed no measurable difference in particle size distributions.

The fuel used for all tests was #2 diesel fuel with nominal sulfur level of 350 ppm. To dope the fuel with iron, small amounts of ferrocene powder/crystals, i.e.  $(C_5H_5)_2Fe$ , were measured using a milligram scale and mixed with about 200 ml of fuel in a beaker. This was heated on a hot plate to 60 °C and stirred with a magnetic stirrer for 30 min until all the ferrocene was dissolved. The solution was then blended with the appropriate amount of diesel fuel to achieve the desired doping level. For example, mixing 4 gm ferrocene (0.301 mass fraction Fe), with 20 kg fuel yielded about 60 ppm of Fe in the fuel.

### 2.2. Particle size measurement using the SMPS

Particle size distributions were measured using an SMPS (Wang & Flagan, 1989). The SMPS system used in this experiment was built in-house and is a modified version of a TSI instrument, consisting mainly of a particle neutralizer (Po210), a “long-column” differential mobility analyzer (DMA), a TSI model 3010 condensation particle counter (CNC), and data acquisition PC. The incoming aerosol enters the system through a critical orifice at a flow rate of 1.0 lpm and filtered sheath air is recirculated in the system at 10 lpm by an adjustable blower. The PC computer interfaces with the DMA voltage supply and scans the voltage from 0 to 10 kV and back, over a 4 min period. The data acquisition stores voltage and particle number counts which are then used to determine size distribution after correction for charge distribution, aerosol residence time and voltage ramping effects.

### 2.3. Single-particle mass spectrometry

A schematic diagram of the SPMS used in this study is shown in Fig. 2, and is slightly modified from the original. The components of the system consist of an aerodynamic lens inlet, three-stage differential pumping system, free-firing dissociation/ionization laser and optics system, linear time-of-flight mass spectrometer, and data acquisition system composed of a high-speed digital storage oscilloscope and a PC. Details of the components and their working principles are described elsewhere (Mahadevan et al., 2002).

The pressure in the inlet tube downstream of the pressure-reducing orifice is 1.6 Torr when the pressure upstream of the inlet is maintained at 1 atm, while the pressure in the first stage vacuum chamber, which is pumped by a 250 l/s turbo molecular pump, is  $2 \times 10^{-2}$  Torr. The second and third stages are pumped with a 1000 l/s turbo pump and a 210 l/s turbo pump, which maintain pressures of  $1 \times 10^{-5}$  and  $6 \times 10^{-7}$  Torr, respectively, when the system is sampling. At a distance of 30 mm downstream of the aerodynamic lens inlet, the narrowly focused aerosol beam intersects a laser beam at the center of the extraction plate (see Fig. 2). The laser used in the system is a frequency-doubled Nd:YAG laser operated at 10 Hz in the internal Q-switch mode. The laser energy measured before the laser entrance window of the mass spectrometer is about 100 mJ/pulse. The power density of a 5 ns laser pulse focused at the center of the extraction region (see Fig. 2) is estimated to be approximately  $2.8 \times 10^{10}$  W/cm<sup>2</sup> assuming the beam diameter at the focal point is 0.3 mm. Each laser shot is detected with a photodiode sensor to initiate time-of-flight measurement in the data acquisition system.

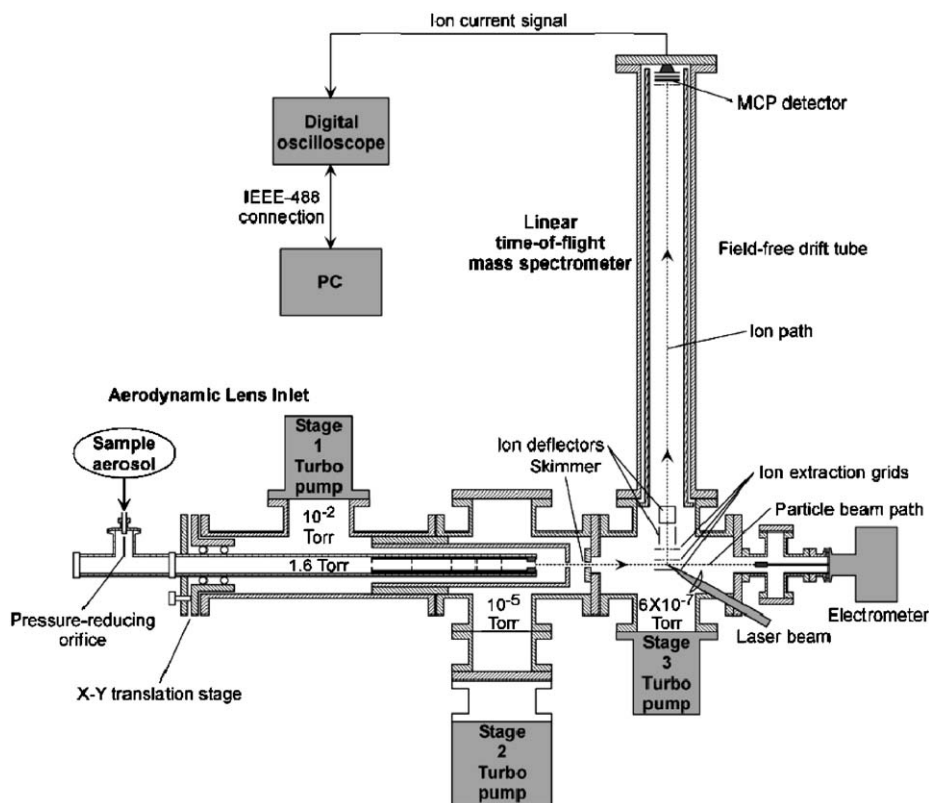


Fig. 2. Schematic of the linear time-of-flight single particle mass spectrometer (SPMS).

When the laser hits and disintegrates a particle, atomic ions comprising the particle are generated in the extraction field of the mass spectrometer. The positive ions with one or more elemental charges are accelerated along the 1 m long, linear-time-of-flight tube and detected by microchannel plates. The temporal ion signals are captured by a 500-MHz digital storage oscilloscope and stored on PC via GPIB connection.

Examples of typical particle mass spectra are shown in Fig. 3a–c. Note that although there are some molecular fragments ( $C_x$ ,  $N_2$ ,  $O_2/S$ ), the particles were generally ablated to their elemental constituents. The peaks at  $m/z = 32$  are likely a combination of  $O_2$  derived from dilution air and sulfur derived from the fuel or oil. Though much of the sulfur leaves the tailpipe as vapor-phase  $SO_2$ , a few percent of sulfur is known to convert to particulate sulfate and could thus contribute to that peak. We also considered the effect of background (BG) ions or molecules such as  $N_2$  and  $O_2$ , which may give or take electrons via collision with primary ions or neutrals generated from the particle. This so-called “matrix effect” or “charge transfer effect” is likely not significant here, for the following reasons. First, there are relatively few collisions due to the very low pressure surrounding the laser focal volume. Second, the mean absolute BG signal intensity in the presence of particles is quite similar to that with no particles introduced to the SPMS, i.e. the BG signal originates from direct ionization of BG due to the high intensity of the laser used.

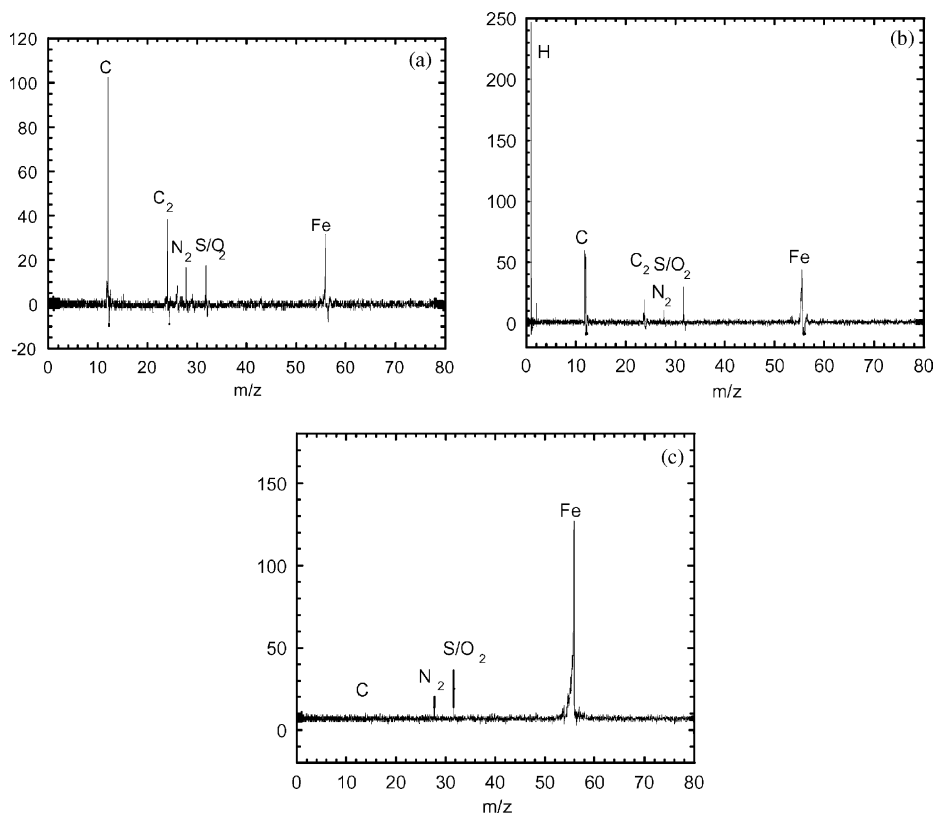


Fig. 3. Three classified examples of Diesel SPMS: (a) elemental carbon, (b) organic carbon, and (c) pure iron coated with very thin carbon.

Thousands of such spectra were collected during the course of this work. Each spectrum is unique, as is each particle. Key to our analysis of the particles is the application of customized software developed for quickly sorting data files, and providing statistical analysis of the relative size of all spectral peaks for multiple elements. The software also allows for rejection of “bad hits”, which are spectra containing only BG signals, or dominated by BG noise. For our purposes, all O<sub>2</sub> and N<sub>2</sub> signals were considered to be noise, induced by the presence of air in the aerosol stream.

#### 2.4. Correlating particle size with SPMS signal intensity

In principle if all atoms in the particle were converted to ions and the flight tube transported all ions to the microchannel plate, the integrated ion spectra would yield a direct mass measurement for the particle. However, we know that the above constraints are never met in our system. We have however developed a way of determining particle size from the SPMS signal intensity.

This was done using the following procedure. The transmission efficiency of nanoparticles through the lens and skimmers was first measured as a function of size by measuring the electrical current generated by size-selected charged particles before and after the inlet assembly. Next, PSL spheres of

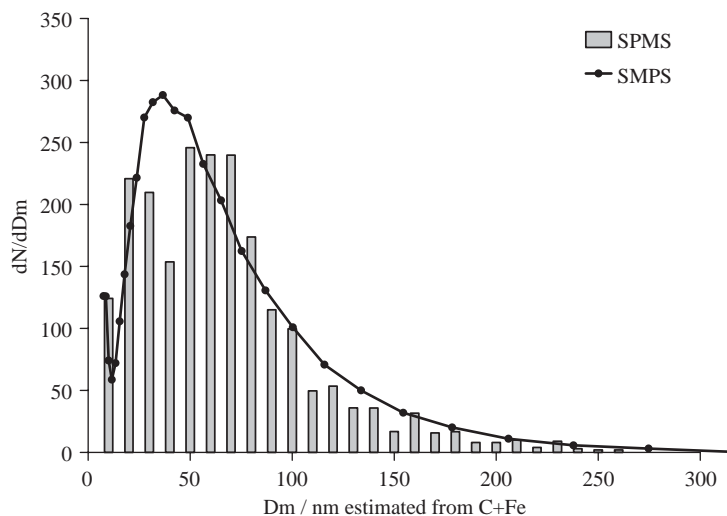


Fig. 4. Comparing SMPS size distribution and SPMS-derived mobility diameters for Fe-doped diesel exhaust at 0 kW engine load.

known size were sampled and the SPMS signal intensity was correlated with their volume, yielding a correction factor. Finally, the size distribution of the diesel aerosol was measured using an SMPS, while numerous single-particle mass spectra were collected using the SPMS. The signal intensity of the spectra were used along with the correlation factor to estimate the original particle volume. It is notable that the correlation is not linear but rather is best fitted by a power function. This is ascribed to the size-dependent ion losses during their transport from the laser focus to the detector, due to the size dependence of energetic ion formation. Details on this topic will be described in subsequent publications (Lee, Park, & Zachariah, 2005). We found the correlation factor is not material dependent (see Fig. 2 of the reference).

From our measured size correlation factors, we know  $D_v = 29.135PA^{0.71}$ , where PA is the total peak area of the SPMS signal. Using this nonlinear size correlation function, volume-equivalent sizes of original particles were obtained straightforwardly from a large set of mass spectra. The resulting size distribution is then correlated with the original size distribution of particles by dividing the SPMS-measured distribution by the transmission efficiency. Since the mass of diesel exhaust PM has been shown to be well correlated with mobility size (volume =  $5.1523D_m^{2.31}$ ) (Park, Cao, Kittelson, & McMurry, 2003), the volume data (SPMS) was converted to  $D_m$  to allow direct comparison between results from the SPMS and the SMPS. The mobility size distribution for the volume data from the SPMS ( $dN/dD_m$ ) is then obtained by counting the number of mass spectra of particles whose size lies in each constant bin and then dividing the number by the bin size. As for the SMPS data, it is usually presented as  $dN/d\log D_m$  rather than  $dN/dD_m$  due to its intrinsic size-dependent mobility bandwidth ( $dZ_p$ ). Since the size/bin allocation of particles passing through the DMA slit is proportional to their size, converting from  $dN/d\log D_m$  (SMPS) to  $dN/dD_m$  requires multiplying by a constant  $\Delta \log D_m$  (0.06235) and then dividing by the size  $D_m$ , i.e. the relation  $dN/dD_m = dN/d\log D_m(\text{SMPS}) / (D_m \times \ln(10))$  is used in converting from  $dN/d\log D_m$  (SMPS) to  $dN/dD_m$  for direct comparison of the two data sets as shown in Fig. 4. Note that since the y-axis units



of the two distribution curves were not the same, we normalized them by multiplying each data point by the ratio of peak values for the two curves.

The match of the two size distributions indicates reasonable correlation of signal intensity to particle size and the agreement is especially good for the larger particles. The smaller particles, due to their high diffusivity, have poor collimation in the aerodynamic lens, and therefore poor transmission efficiencies to the ablation laser. This is evident in that the mobility sizing (SMPS) measurements under both engine load conditions (especially for the higher doping case) show high concentrations of particles less than 30 nm for which our mass spectrometer only occasionally registered hits. It should be noted that the electrical current measurements, used for the estimation of transmission efficiency, were lower for smaller particle sizes and were eventually comparable to noise for particles less than 30 nm, partly due to low concentration of nanoparticles in the calibration aerosol. The transmission efficiency was thus assumed to be constant in the range 10–30 nm.

### 3. Results and discussion

In this section, we discuss the determination of particle composition from the SPMS data, with an eye toward quantifying the distribution of iron on particles of various sizes. For these experimental conditions, the vast majority of the particulate matter consists of H, C and Fe, so we will focus on those three elements. The relative proportions of these elements were derived from the ratios between peak areas in the particle mass spectra, the validity of this assumption has been reported in our prior work (Mahadevan et al., 2002). We thus determined both the size and elemental composition for each of many particles and used this to investigate the distribution of a particular element (say Fe) across the measured particle size range.

#### 3.1. Particle size distribution

Fig. 5a shows that when the fuel is doped with 60 ppm iron, the size distribution of particles contains a distinct nuclei mode that increases with engine load. This increase in self-nucleated metal particles reflects higher metal throughput, since the increase in load results in higher fuel flow rates and thus higher metal throughput. As the doping rate is reduced to 20 ppm (Fig. 5b), the iron content is lowered and the nuclei mode eventually disappears at 0 kW engine load as illustrated in the figure. Note the difference of the vertical axis in Fig. 5 ( $dN/d\log D_m$ ) compared to  $dN/dD_m$  in Fig. 4. For both doping levels (Fig. 5a and b), the size distribution is strongly bimodal in the range measured by the SMPS and the dilution-corrected total number concentrations vary from about  $5 \times 10^7$  to about  $5 \times 10^8$  #/cc (higher numbers being reflective of the increasing number of nuclei-mode particles at high engine load). The accumulation-mode particles are shown to decrease as load (and thus both engine temperature and metal content) goes up, especially during the initial increase from 0 to 4 kW load. That is not surprising since this engine produces less soot at higher loads, but it is also possible that the metal-enhanced oxidation of carbon may play a role as observed in an earlier work (Jung, Kittelson, & Zachariah, 2005). The role of iron content on soot oxidation and particle morphology will be described in detail in a follow up study. For this work, we will focus mainly on the role of condensation, self-nucleation and coagulation in distributing metal onto particles.

We surmised that if the appearance of the nuclei mode is directly attributable to self-nucleation of iron then there should be a direct correlation between the mass flow rate of Fe through the system and the

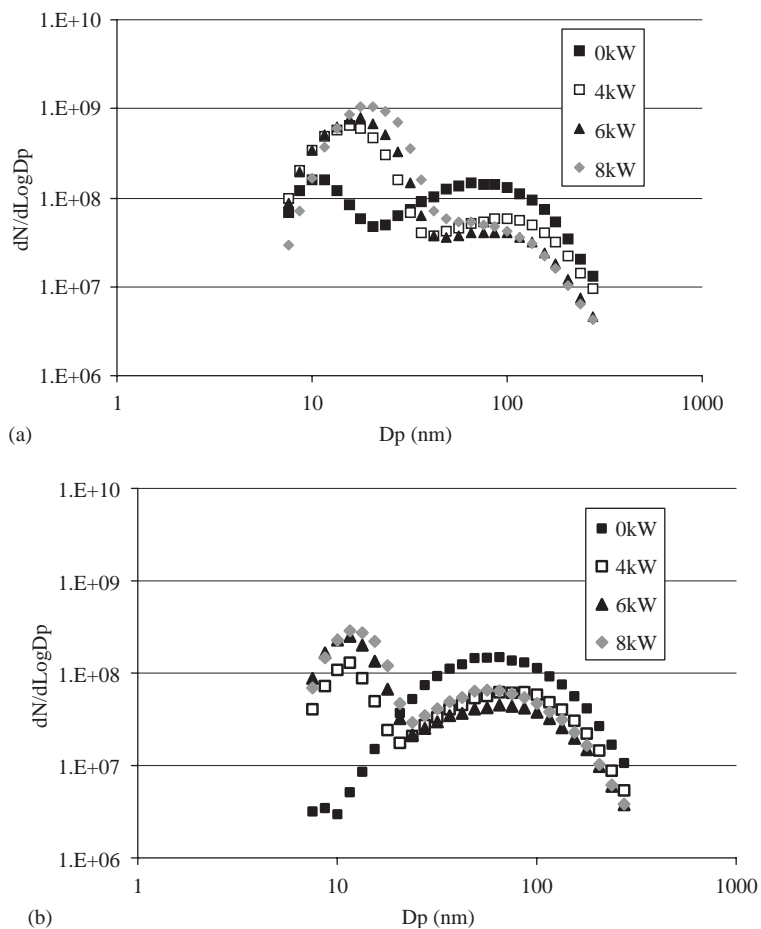


Fig. 5. Number-weighted size distribution of diesel particles for different engine loads: (a) with 60 ppm iron added to the fuel, and (b) with 20 ppm iron added to the fuel.

volume of nuclei-mode particles ( $\sim$ less than 20 nm) for each condition. Fig. 6 shows the relationship between Fe mass flow rate and total volume of particles less than 20 nm measured by the SMPS, i.e. as in Fig. 5, for several different engine conditions. The Fe mass flow rate was obtained for each operating condition as the product of doping level and fuel flow rate. It is evident from the first two data points on the left that there is a “baseline” volume of small particles for this engine that is independent of the presence of metal. This baseline we attribute to the “tail” of the non-iron containing accumulation mode.

The rest of the data show that starting at a “threshold” value of about 0.025 g/h of Fe flow, the volume (and thus mass) of self-nucleated particles increases linearly with increase in the Fe throughput. This threshold value corresponds to a critical Fe/C ratio at which self-nucleation of metallic particles first begins. Further increase in Fe input simply adds to the number and size of such nucleated particles. This is an important result in view of new engine technology designed to meet future emission standards, which employs precise control of high-pressure fuel injection to reduce  $\text{NO}_x$  and particulate (carbon) emissions. These “cleaner” engines, which have a reduced carbon particulate matter emission, will

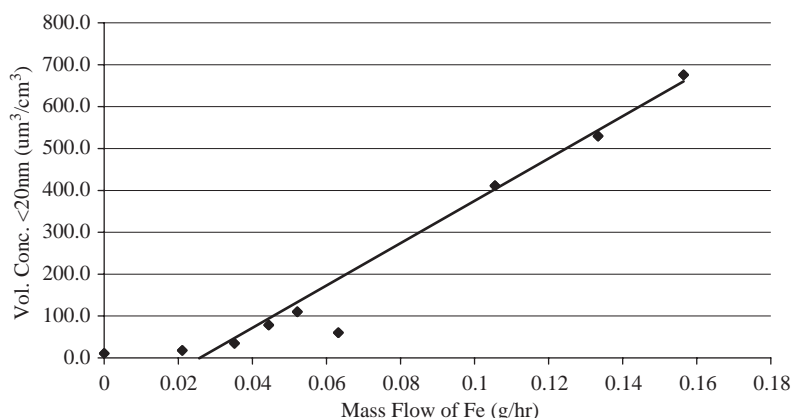


Fig. 6. Total volume of nuclei-mode particles (< 20 nm) as a function of Fe feed rate.

presumably have increases in the metal to carbon ratio and enhance the likelihood for formation of metal nanoparticles.

### 3.2. Particle mass spectra sorted by class

Due to the wide distribution of aerosol composition as observed in the mass spectra, we found it useful to sort the spectra by general class. To do this we counted on previous knowledge of particle morphology in the nuclei and accumulation modes of typical diesel exhaust. The nuclei mode of DPM is generally considered to consist of two particle types; nonvolatile inorganic ash that nucleates at high temperatures in the engine (Abdul-Khalek et al., 1998; Kittelson et al., 2002), and condensed volatile materials such as sulfates and unburned fuel or oil which self-nucleate later during the dilution/cooling of the exhaust aerosol (Sakurai et al., 2003). The accumulation mode on the other hand, which would be the third type of particle, is said to consist mainly of “spherules”, i.e. primary particles of elemental carbon (EC), coagulated into agglomerates, with other materials adsorbed onto the surface. To verify this for our case, we took DPM samples for TEM/EDS analysis using a low-pressure cascade impactor (LPI) (Hering, Friedlander, Collins, & Richards, 1979). Fig. 7 shows a TEM image which contains all three of the above-mentioned particle types. This sample was taken from the final impactor plate of the LPI and represents particles with aerodynamic diameter around 50 nm. EDS analysis of the two small, dense particles in Fig. 7 indicate that they are composed mainly of iron.

For the purposes of the following discussion, the particle mass-spectra were sorted into three basic particle types as follows. Note that the values of C, H, and Fe, are molar ratios and are obtained from the areas under the elemental peaks of the individual mass spectra.

- (1) EC particles are defined as those where  $H/C < 1$ . These are particles containing greater relative amounts of EC (typically agglomerates of primary carbon spherules).
- (2) OC particles are defined as those where  $H/C > 1$ . They are typically nanoparticles containing fuel or oil residues rich in OC, i.e. rich in hydrogen.
- (3) “Pure iron” particles are those where  $Fe/C > 10$ . These are the nanoparticles of iron (presumably self-nucleated in the engine).

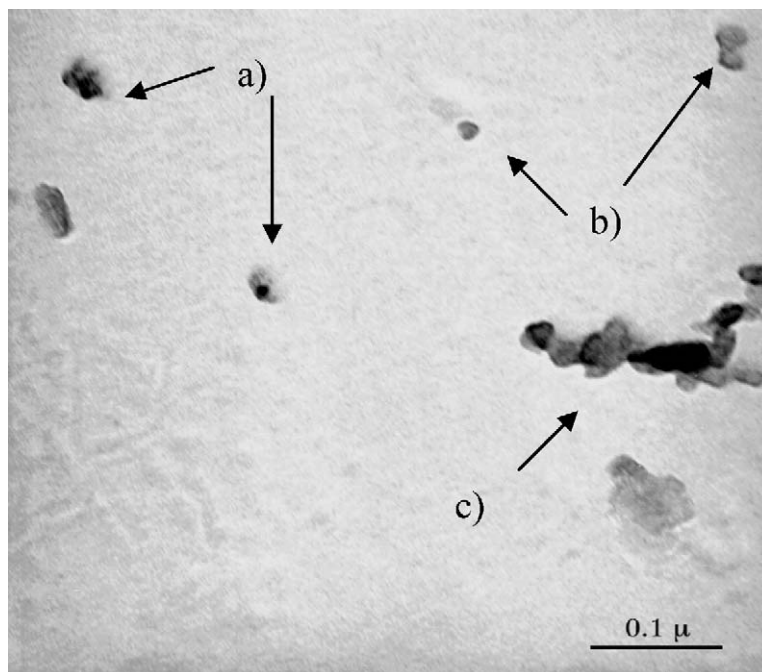


Fig. 7. TEM micrograph of size-selected DPM, showing: (a) nucleated iron particles, (b) hydrocarbon particles, and (c) chain agglomerate particle. Note: 6 kW load, 60 ppm iron doping rate.

Before looking at detailed particle stoichiometry, we present the SPMS results for these three particle types, in terms of the frequency distribution of each type as a function of particle size. Figs. 8 and 9 show the number-weighted mobility size distributions, for each of the three particle types at two different engine conditions and two different doping rates of iron. Note that particle sizes presented in all figures for the SPMS are mobility sizes transformed from  $D_v$ . Although these particle types are by no means definitive, some significant trends are noticeable.

Fig. 8a shows that at low engine load and high ferrocene doping rate, the EC particles are widely distributed, with a peak at around 70 nm, and constitute the bulk of the particulate material, which coincides with the distribution of agglomerate particles, i.e. the accumulation-mode particles shown in Fig. 5. Fig. 8a also shows that the OC particles are distributed in the lower size range (< 50 nm), i.e. the lower-side tail of the accumulation mode. Under the conditions for Fig. 8a we see virtually no “pure iron” particles. This is probably due to higher carbon generation at low load, preferentially facilitating Fe adsorption onto carbon particles rather than nucleation of Fe. The result is that at the lower load, the nuclei-mode iron particles as measured by mobility diameter (Fig. 5a), are fewer in number and almost all less than 30 nm in diameter, and in that range the mass spectrometer has poor particle transmission efficiency.

At higher engine load, the increase in Fe throughput combined with inherent soot reduction yields a higher Fe/C ratio, so the pure iron particles have increased in number and grown in size to a point where the aerodynamic lens is able to transmit them more efficiently to the ionization laser. Fig. 8b shows that at 6 kW engine load, about 9% of the detected particles (by number) are pure iron nanoparticles. Note that

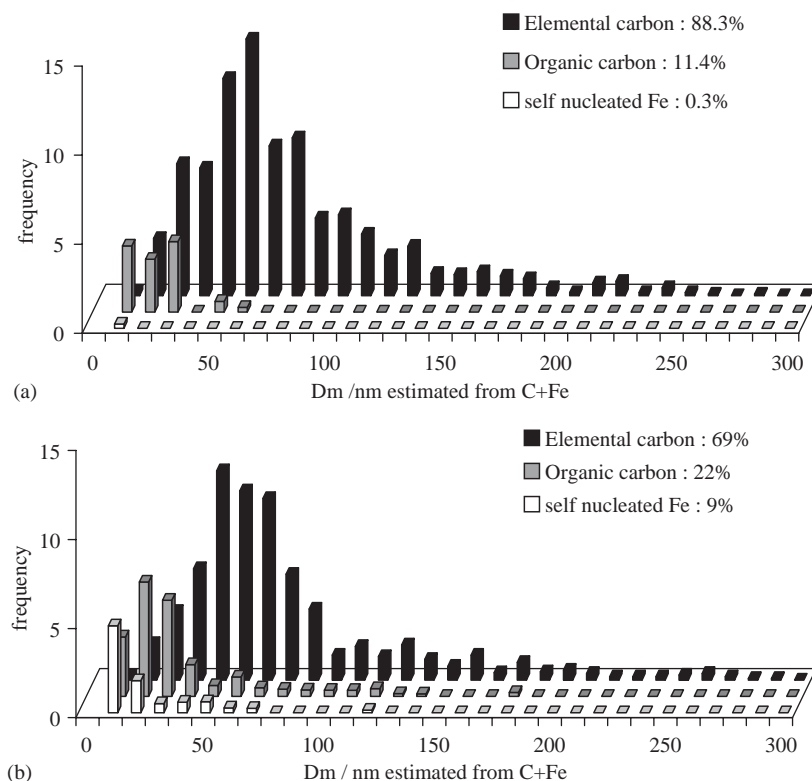


Fig. 8. Size distributions for three classes of diesel exhaust particles with high-Fe doping: (a) 0 kW load, (b) 6 kW load. Note: Percent distributions refer to frequency of occurrence.

in this figure the size distribution of the EC particles has not changed significantly, which is consistent with the SMPS measurement in Fig. 5(a).

For the lower iron doping case (Fig. 9), size distributions are similar to those for the higher doping case (Fig. 8). Again at the low load, we see an absence in the mass spectra of pure iron particles and as discussed previously we attribute this to a transmission efficiency effect. The lower load gives a wider size distribution of the EC particles (Fig. 9a) and one might be tempted to see in the data a bimodal distribution. It should be kept in mind that the definition we employed to distinguish organic and EC is arbitrary and the bimodal-looking distribution may be associated with particles that are of an OC type but did not fulfill our definition of H/C of  $> 1$ . A further discussion of that point is presented in the next section.

In general we see that the appearance of self-nucleated particles is promoted at high engine load because of the higher fuel flow rate and therefore higher iron injection rate, combined with lower carbon (soot) content. The effect of increasing the iron doping rate is to directly increase the iron content in the nuclei mode, while the effect of engine load is coupled with doping rate via the rate of fuel flow. The combined effect of both these influences is perhaps best reflected in Fig. 6. The relative number of OC particles was shown to be greater for the higher engine load cases which can be attributed in part to reduced emissions of EC as engine load goes up (somewhat unique to this engine), which results in apparent increase in OC

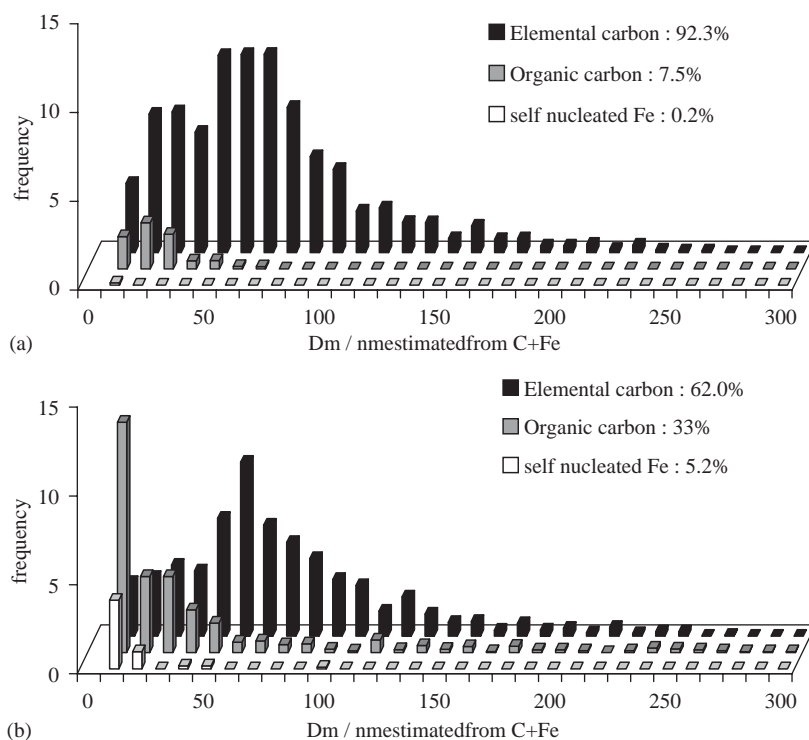


Fig. 9. Size distributions for three classes of diesel exhaust particles with low-Fe doping: (a) 0 W load, and (b) 6 kW load. Note: Percent distributions refer to frequency of occurrence.

relative to EC. Further discussion of the latter point will be included in the following section. The relative frequency of elemental and OC particles varied somewhat, possibly due to the fact that our distinction between these two classes based on a fixed ratio of H/C is somewhat arbitrary and the fact that on a shot-to-shot basis, hydrogen content of particles varied greatly.

### 3.3. Detailed elemental composition

In the following discussion, we look more closely at the composition of the diesel exhaust particles. We present results (Figs. 8–14) that illustrate the analysis of numerous mass spectra to observe trends in particle properties, namely the amount of various elements in each particle.

#### 3.3.1. Elemental carbon particles

The data in Figs. 8 and 9 show that the distribution of EC particles measured by the mass spectrometer is similar to the accumulation mode of the particle size distribution as measured by the SMPS, and is relatively independent of iron addition. It is also notable that as load and thus Fe throughput increases, the absolute number of these accumulation-mode particles decreases (note the difference between the no-load and 4 kW cases in Fig. 5). Such reduction is somewhat expected since this engine produces less soot at higher loads, but it is also possible that metal-enhanced oxidation of carbon is taking place. This is suggested by earlier studies (Bonczyk, 1991; Bagley et al., 1996; Miyamoto, Zhixin, Harada, Ogawa, &

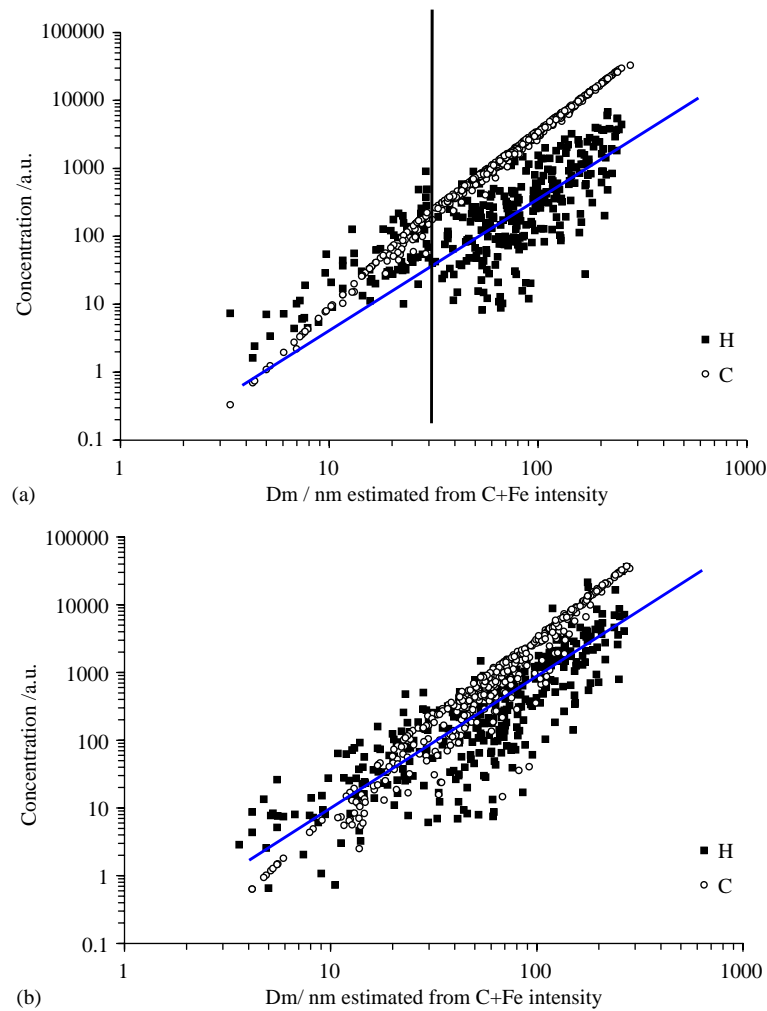


Fig. 10. Size dependence of carbon and hydrogen in diesel exhaust particles for the case of high-Fe doping: (a) 0W load, and (b) 6kW load. (Note: solid line through data shows  $D_{m,c}^2$  dependence of elemental concentration.)

Murayama, 1987; Otto, Sieg, Zinbo, & Bartosiewicz, 1980), which describe how the presence of metal deposited onto carbon particles leads to oxidation of carbon late in the combustion process. It may also be related to soot suppression in the early combustion stages as suggested by one study (Miyamoto et al., 1987).

The latter issue is a matter of considerable discussion in the literature. It has been shown that for premixed flames (Ritrievi, Longwell, & Sarofim, 1987), addition of metal triggers the self-nucleation of metal oxide nanoparticles, which form prior to the soot, and in fact enhance soot production by supplying sites for subsequent condensation of carbon, thus encouraging soot formation. On the other hand, laminar diffusion flames, which in theory are more akin to diesel combustion flames, have been shown to display the same behavior, i.e. early generation of metal-oxide nanoparticles (Bonczyk, 1991), but (perhaps due to reduced oxygen availability) this process appears to be limited, leaving sufficient metal vapor in the

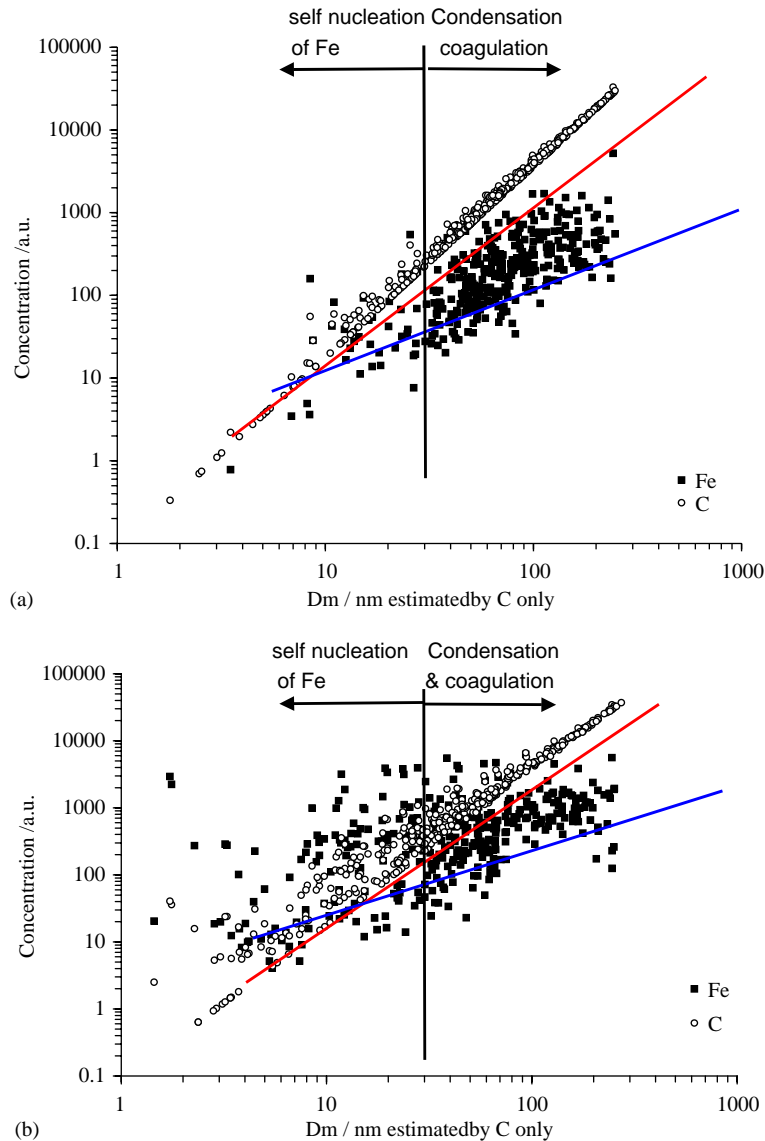


Fig. 11. Size dependence of iron and carbon fractions in diesel exhaust particles for the case of high-Fe doping: (a) 0W load, and (b) 6kW load. (Note that upper line shows  $D_{m,c}^2$  while lower line shows  $D_{m,c}^1$ .)

system to form metal oxide partial coatings on the soot particles, evidenced by their high rate of oxidation later in the flame. Neither of these studies indicated that metal played a role in suppression of soot during the combustion process. However, an earlier study involving diesel engines (Miyamoto et al., 1987), in which soot concentration was measured in the cylinder as a function of crank angle, suggested that during diesel combustion of metal-doped fuel, soot is not only oxidized due to its metallic coating, but that its formation is also suppressed. In that work, however, the soot measurements were not necessarily taken near the main diffusion flame, so it is still unclear whether the data is applicable here.



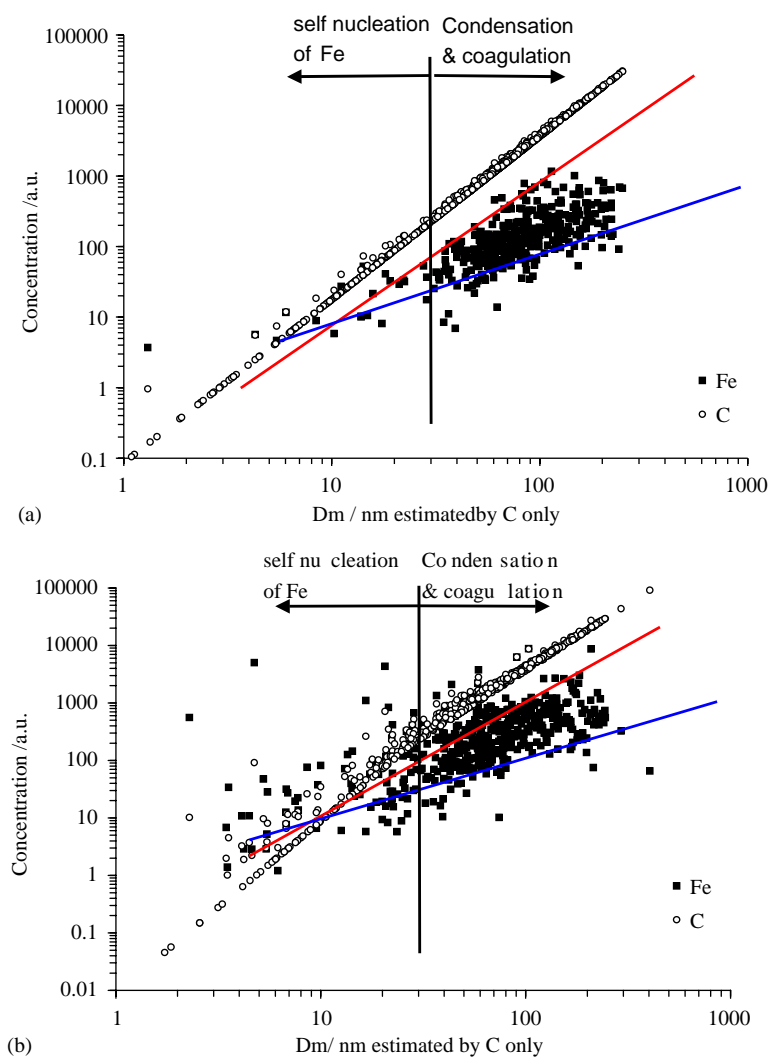


Fig. 12. Size dependence of iron and carbon fractions in diesel exhaust particles for the case of low-Fe doping: (a) 0 W load, and (b) 6 kW load. (Note that upper line shows  $D_{m,c}^2$  while lower line shows  $D_{m,c}^1$ .)

Our definition of EC particles is primarily used to distinguish them from the organic-type carbon particles; however, it should not be used to imply that these particles do not contain iron. In fact many accumulation-mode particles, which are mainly EC, also contain some iron. Such particles will be discussed further in the latter part of this section.

### 3.3.2. Organic carbon particles

OC particles, based on our definition, are more prevalent in the smaller size ranges, which is consistent with a previous observation (Sakurai et al., 2003) that documented the increase in volatile hydrocarbon species on particles of smaller sizes. The existence of these more volatile hydrocarbon species is reflected

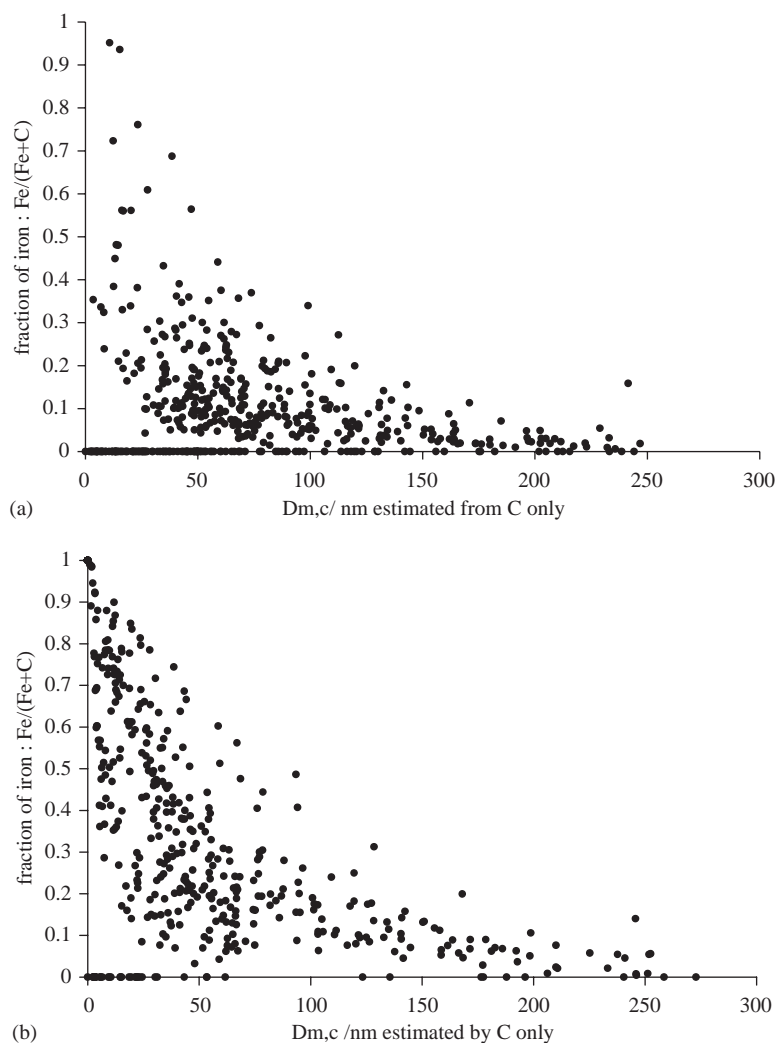


Fig. 13. Size dependence of iron fraction in diesel exhaust particles for the case of high-Fe doping: (a) 0 W load, and (b) 6 kW load.

in the data of Fig. 10a and b, which show the relative amounts of hydrogen and carbon for all hydrogen-containing particles at the higher Fe doping rate. The OC particles, as defined by  $H/C > 1$ , are those data points lying above the carbon curve.

Note that for this and subsequent figures, each point on a graph represents the area under one elemental peak from one unique mass spectrum (i.e. one particle). The x-axis reflects the size of the particle analyzed, i.e. the mobility diameter calculated using the correlation described in the previous section. The values on the y-axis reflect the relative amount of each element determined by calculating the area under that elemental peak. For carbon, due to molecular fragments, we sometimes had more than one peak and in that case the area under all carbon-containing peaks would be summed to give the amount of carbon for that particle. These area summations represent the relative contribution of each element in the particle, and

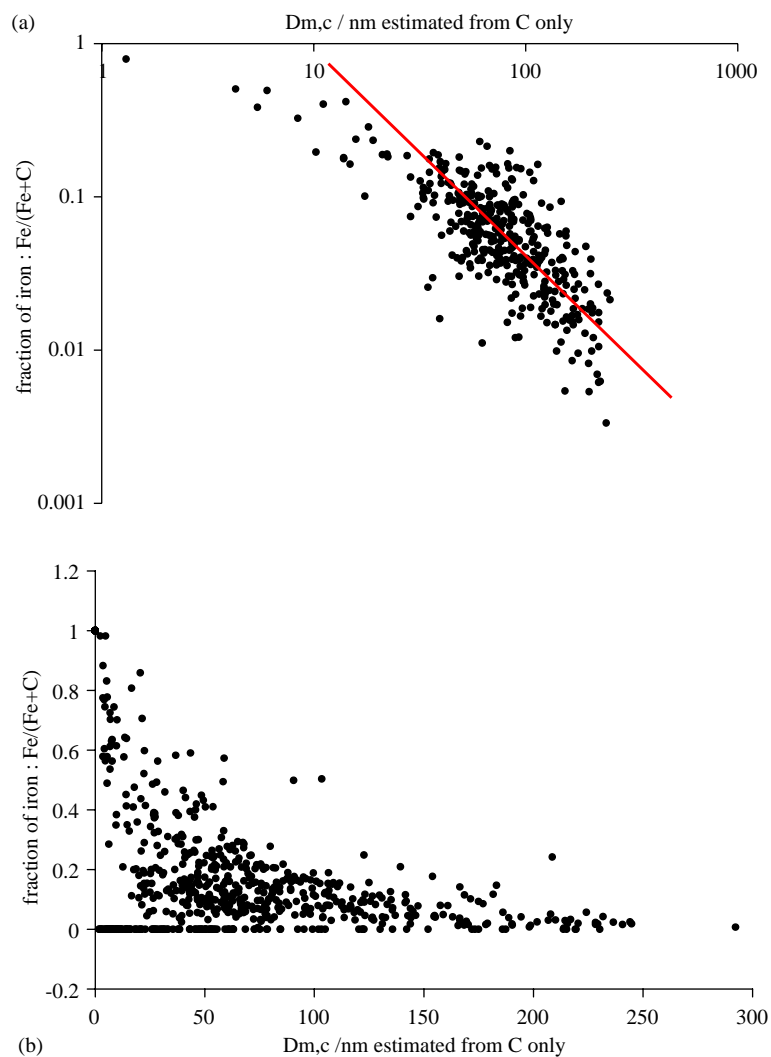


Fig. 14. Size dependence of iron fraction in diesel exhaust particles for the case of low-Fe doping: (a) 0 W load, and (b) 6 kW load. (Note: solid line through data shows  $D_{m,c}^{1.31}$  dependence.)

therefore give mole fraction or particle elemental stoichiometry. The validity of this has been discussed in our previous work (Mahadevan et al., 2002).

We observe in Fig. 10 that the H/C ratios are clearly greater for smaller particles, but the scatter in the data demonstrates how elusive it would be to define a “typical” H/C ratio for diesel particles. The variation in H/C may reflect the locally varied temperature history that the particles underwent, which results in local variation in the (partial) burning of fuel and lube oil, as well as variation in the vapor deposition history.

Note that for particle size estimation we use two different schemes. Since the mean diameter of primary carbon particles is around 25–30 nm, if the measured  $D_v$  is larger than 30 nm, the  $D_v$  is converted to  $D_m$

as described above, while if  $D_v < 30$  nm, we set  $D_m = D_v$ , i.e. we assume the particles to be spherical. For this reason in Fig. 10 and subsequent figures there is a slight inflection in the carbon curve at 30 nm.

The solid line in Fig. 10 was drawn to indicate that the amount of hydrocarbon deposited to the preexisting iron-bearing carbon particles scales as  $D_m^2$ , i.e. approximately to the surface area of the accumulation-mode PM. This might imply that a significant portion of the volatile hydrocarbon condenses near the tail pipe, before and during dilution cooling. Under those conditions the very small-sized PM would undergo free-molecular condensation, i.e. where condensation rate is proportional to the surface area of particle cores. At the lower doping level, this same dependence on size ( $D_m$ ) was found at both engine loads (not shown here). Note that the horizontal axis in the figures corresponds to mobility size of composite particles estimated from the sum of carbon and iron peak areas.

### 3.3.3. Pure iron particles

We noted earlier that the “pure iron” particles are detected by the SPMS only at high engine loads. At this condition, the quantity of Fe more than doubles due to increased fuel flow rate, while the soot concentration decreases. The combined effect heightens the Fe/C ratio, effectively increasing the supersaturation ratio of iron vapor in the combustion chamber, in turn causing the nuclei-mode particles to grow larger and more numerous. At the size of around 25–30 nm, they are large enough to penetrate the aerodynamic lens and therefore are detectable. This is best seen in Fig. 11a and b, which show, for the higher doping rate, higher iron levels for the especially small particles. At the lower engine load (Fig. 11a), the data shows a tightly banded distribution of iron and a relatively low iron fraction over much of the particle size range, i.e. lower engine loads produce less iron relative to carbon because the engine produces more carbon and less fuel is consumed to provide iron. In comparison, Fig. 11b shows that at higher engine load, many of the smaller particles lie above the carbon curve, suggesting that they are “pure iron” particles, while many of the larger particles have iron content similar to the low load case. Overall, the relative amount of Fe is also higher and more variable over the entire size range for the high load case. The latter can be explained by the dominance of mutual coagulation, i.e. over nucleation and condensation, between the three types of particles.

Note that in the figure the mobility size corresponds to carbon core mobility diameter that was estimated from the carbon peak area only. This was done because we wanted to investigate whether or not the Fe vapor condenses onto preexisting carbon, not the whole PM size. We postulated that the iron is condensed to the preexisting carbon core or self-nucleate inside the engine cylinder due to its very low vapor pressure. If this is the case, the behavior of particles may lie in the continuum regime, for which the deposition rate of Fe is proportional to diameter (Friedlander, 1977). The slope of the plotted data Fe vs  $D_{m,c}$  lies indeed between  $D_{m,c}^1$  and  $D_{m,c}^2$  (indicated by lower and upper solid lines, respectively), which is obviously smaller than the slope of H vs  $D_m$  in the previous figure. This is not surprising because inside the engine the pressure is very high, moving the particle behavior toward continuum conditions, where the deposition rate of Fe is proportional to  $D_{m,c}^1$ . The results might reflect that the present condition for incorporating Fe is fairly close to the continuum regime.

For the lower doping rate (Fig. 12a, b), the low load condition (Fig. 12a) yields the lowest Fe/C ratios as well as the tightest grouping of data. This tight grouping suggests lack of coagulation effects, and the data points collapse more closely to the lower solid line ( $D_{m,c}^1$ ) representing pure condensation in the continuum regime as explained above. For the higher load case (Fig. 12b), small particles of pure iron are evident (those above the carbon curve), and the effect of their coagulation with larger carbon particles makes the data grouping less tight.

Plotting the Fe fraction of the DPM against  $D_{m,c}$  clearly shows the relationship between iron content and particle size. Fig. 13a shows that at low load and high Fe doping, the iron content increases sharply for smaller particles. At high load (Fig. 13b) the trend is similar but significantly more particles are high in iron while very few (those on the  $x$ -axis) have no iron. In contrast to Fig. 13a, the data of Fig. 13b show a similar behavior of iron content, but with increased data scatter. The scatter is believed to be a result of a trend toward coagulation dominance in the aerosol system, which would tend to scramble the distribution. This coagulation is driven by the increase in size and number of self-nucleated iron particles observed at the higher load, i.e. when there is more iron available.

The evidence of condensation is seen most clearly at low Fe doping (Fig. 14a, b). Similar to the high doping case, the Fe content increases sharply for smaller particles as seen in Fig. 14b. The data for the low load (Fig. 14a) represent the lowest Fe/C conditions of all the cases we investigated and for this reason we graphed them in log scale to better show the diameter dependence of iron content under those low-Fe conditions, where little if any self-nucleation is taking place. Note that the trend line reflects  $D_{m,c}^{1.31}$ , suggesting condensation in the continuum regime. This supports the argument that prior to self-nucleation, iron is depositing onto particles via condensation.

In general we see that higher iron content either through higher doping or the indirect effect of higher engine loads (increased fuel flow rate) tends to produce more scatter in the iron size distribution. At low iron doping the results are consistent with a heterogeneous condensation of iron onto carbon. At the higher iron concentrations, we observe a much larger nucleation mode consistent with a higher supersaturation of iron vapor which favors homo vs. heterogeneous nucleation. These nuclei-mode particles will preferentially coagulate with the accumulation-mode particles and will scramble the tight iron distribution most clearly seen in Fig. 12a.

#### 4. Conclusions

The origin of adverse health effects associated with DPM is still unclear. To that end, we were motivated by a need to quantify the metals associated with DPM, especially the ultrafine portion. In this work, we report on the application of single-particle mass spectrometry to obtain the size- and composition-resolved statistics needed to gain insight into the formation mechanisms of metal-bearing diesel particles, for the full size range of DPM, including nanoparticles. For our assessment the DPM is divided into three main particle types: self-nucleated metal-rich nanoparticles, ultrafine particles rich in OC, and larger EC agglomerates containing small amounts of metal. Note that all three types will inherently contain a certain amount of adsorbed hydrocarbons.

At the lowest metal doping level, below the onset of apparent self-nucleation, metal to carbon ratio as a function of size is well fitted with a  $1/D_p$  curve, implying that for this case, metal condensation onto preexisting carbon is a dominant mechanism for DPM to contain metal. In contrast, at higher doping level and higher engine load (higher flow rates of metal-doped fuel), the metal to carbon ratio is greatly scattered over the entire size range, suggesting that coagulation with metal-rich nanoparticles dominates the distribution of metals. Somewhere between these two extremes lies a set of conditions which triggers the onset of metal self-nucleation. This threshold condition will be dependent on the quantity of metal vapors in the combustion chamber, the cylinder temperature, the adiabatic cooling rate and the particle surface area available for vapor deposition. Changes in these parameters will directly affect the way in which metals are distributed in the DPM.

In this work, we demonstrated that in addition to the volatile nanoparticles often generated by diesel engines, it is also possible for non-volatile (and potentially metallic) nanoparticles to form. Under conditions in which soot formation is reduced, the relative abundance of inorganic species will increase, consequently increasing the probability for self-nucleation of metallic species. We also demonstrated how metals may potentially be apportioned on various types of particles due to surface deposition and coagulation. The results have potentially significant implications in terms of assessing the toxicity of DPM under various engine operating conditions.

## Acknowledgements

Partial support for this work came from the DURINT Army Center for NanoEnergetics Research (Dr. D. Mann—program manager). The SPMS was constructed from a National Science Foundation equipment grant (Dr. Mike Roco—program manager). D. Lee was partly supported by Pusan National University Research Grant and Core Environmental Technology Development Project for Next Generation (Project No. 102-041-029). NIOSH-Spokane Research Lab provided equipment contributions and a student scholarship for A. Miller.

## References

- Abdul-Khalek, I. S., Kittelson, D. B., & Brear, F. (1999). *The influence of dilution conditions on diesel exhaust particle size distribution measurements*. Society of Automotive Engineers Technical Paper, 1999-01-1142:1–9.
- Abdul-Khalek, I. S., Kittelson, D. B., Graskow, B. R., Wei, Q., & Brear, F. (1998). *Diesel exhaust particle size: Measurement issues and trends*. Society of Automotive Engineers Technical Paper, 980525:1–14.
- Appel, B. R., & Tokiwa, Y. (1981). Atmospheric particulate nitrate sampling errors due to reactions with particulate and gaseous strong acids. *Atmospheric Environment*, 15, 1087–1089.
- Bagley, S. T., Baumgard, K. J., Gratz, L. D., Johnson, J. H., & Leddy, D. G. (1996). *Aftertreatment device effects on diesel emissions*. Health Effects Institute, Cambridge, MA, Research report no. 76.
- Bonczyk, P. A. (1991). Effect of ferrocene on soot in a prevaporized iso-octane/air diffusion flame. *Combustion and Flame*, 87, 233–244.
- Costa, D. L., & Dreher, K. L. (1997). Bioavailable transition metals in particulate matter mediate cardiopulmonary injury in healthy and compromised animal models. *Environmental Health Perspectives*, 105(5), 1053–1060.
- Donaldson, K., & Stone, V. (2003). Current hypotheses on the mechanisms of toxicity of ultrafine particles. *Annali dell' Istituto Superiore di Sanita*, 39(3), 405–410.
- Du, C. J., Kracklauer, J., & Kittelson, D. (1998). *Influence of an iron fuel additive on diesel combustion*. Society of Automotive Engineers Technical Paper, 980536:1–13.
- Flynn, P., Durrett, R., Hunter, G., Loye, A., Akinyemi, O. C., Dec, J., & Westbrook, C. (1999). *Diesel combustion: An integral view combining laser diagnostics, chemical kinetics, and empirical validation*. Society of Automotive Engineers Technical Paper, 1999-01-0509:1–14.
- Friedlander, S. K. (1977). *Smoke dust and haze* (p. 251). New York: Wiley.
- Hering, S., Friedlander, S., Collins, J., & Richards, W. (1979). Design and evaluation of a new low-pressure impactor (Part 2). *Environmental Science and Technology*, 13(2), 184–188.
- Higgins, K., Jung, H., Kittelson, D. B., Roberts, J. T., & Zachariah, M. R. (2002). Size-selected nanoparticle chemistry: Kinetics of soot oxidation. *Journal of Physical Chemistry*, 106(1), 96–103.
- Jung, H., Kittelson, D.B., & Zachariah, M.R. (2005). The influence of cerium additive on ultrafine diesel particle emissions and kinetics of oxidation. *Journal of Combustion and Flame*, in press, available online April 30, 2005.
- Kittelson, D. (1998). Engines and nanoparticles: A review. *Journal of Aerosol Science*, 29(5/6), 575–588.

- Kittelson, D., Johnson, D., & Watts, W. (2002). *Diesel aerosol sampling methodology*, CRC E-43 final report available at <http://www.crcao.com>.
- Kittelson, D. B., Johnson, J., Watts, W., Wei, Q., Drayton, M., Paulsen, D., & Bukowieki, N. (2000). *Diesel aerosol sampling in the atmosphere*. Society of Automotive Engineers Technical Paper, 2000-01-2212:1–8.
- Lee, D., Park, K., & Zachariah, M.R. (2005). Determination of size distribution of polydisperse nanoparticles using single particle mass spectrometry: The role of ion kinetic energy. *Aerosol Science and Technology*, 39, 162–169.
- Mahadevan, R., Lee, D., Sakurai, H., & Zachariah, M. R. (2002). Measurement of condensed-phase reaction kinetics in the aerosol phase using single particle mass spectrometry. *Journal of Physical Chemistry A*, 106, 11083–11092.
- Miyamoto, N., Zhixin, H., Harada, A., Ogawa, H., & Murayama, T. (1987). Society of Automotive Engineers Technical Paper, 871612:1–7.
- Otto, K., Sieg, M. H., Zinbo, M., & Bartosiewicz, L. (1980). *The oxidation of soot deposits from diesel engines*. Society of Automotive Engineers Technical Paper, 800336:277–289.
- Park, K. H., Cao, F., Kittelson, D. B., & McMurry, P. H. (2003). Relationship between particle mass and mobility for diesel exhaust particles. *Environmental Science and Technology*, 37(3), 577–583.
- Ritrievi, K. E., Longwell, J. P., & Sarofim, A. F. (1987). The effects of ferrocene addition on soot particle inception and growth in premixed ethylene flames. *Combustion and Flame*, 70, 17–31.
- Sakurai, H., Tobias, H. J., Park, K., Zarling, D., Docherty, K. S., Kittelson, D. B., McMurry, P. H., & Ziemann, P. J. (2003). On-line measurements of diesel nanoparticle composition and volatility. *Atmospheric Environment*, 37, 1199–1210.
- Stratakis, G. A., & Stamatelos, A. M. (2003). Thermogravimetric analysis of soot emitted by a modern diesel engine run on catalyst-doped fuel. *Combustion and Flame*, 132, 157–169.
- Suess, D. T., & Prather, K. A. (1999). Mass spectrometry of aerosols. *Chemical Review*, 99, 3007–3035.
- Tobias, H. J., Kooiman, P. M., Docherty, K. S., & Ziemann, P. J. (2000). Real-time chemical analysis of organic aerosols using a thermal desorption particle beam mass spectrometer. *Aerosol Science and Technology*, 33, 170–190.
- Utell, M. J., & Frampton, M. W. (2000). Acute health effects of ambient air pollution: The ultra-fine particle hypothesis. *Journal of Aerosol Medicine*, 13, 355–359.
- Wang, S. C., & Flagan R. C. (1989). *Scanning electrical mobility spectrometer*. Division of Engineering and Applied Science, CA Institute of Technology, Pasadena, CA, (pp. 138–178).